

Tunable Frequency Selective All-Dielectric High Incident Angle Terahertz Absorbers with High Symmetry

ASC Report by Maximilian Williams (u6338634)

Abstract

We propose and analyse two novel tunable all-dielectric metasurface frequency selective absorber designs featuring high absorbance for *S* polarized radiation at non-normal angles. These designs use a unit cell structure, containing a high index structure embedded in a low index substrate. Measurements of absorbance and analysis of electric and magnetic resonances is performed by simulation using *CST Microwave Studio*. [13] [3] [2] [12]

Introduction

The ability to selectively absorb electromagnetic radiation is of general importance in optics and practical applications such as detectors. Recently, the study of metamaterials has led to the development of subwavelength near perfect absorbers with both all dielectric and dielectric conductor construction [12] [6] [11]. In particular, the geometric tuning of arrays of all dielectric cylinders has shown great ability to selectively absorb in the THz domain [12] [6]. However, these devices suffer from weaker performance at non-normal incidence, limiting their practical application. There are two architectures of absorbers. Those which are frequency selective, dubbed *resonant absorbers* - and those that are not, dubbed *broadband absorbers*. Generally, broadband absorbers are designed to absorb incident radiation over as wide a frequency and angle range as possible, whereas resonant absorbers are designed to absorb over a small frequency range. Traditionally, broadband absorbers use lossy materials to attenuate incoming radiation, whereas resonant absorbers use excitation within their structure to interfere with incoming radiation [14] (figure 1 (a)). The latter approach has been used in the field of metamaterials to produce two classes of metamaterial, those that are constructed from conductors and those that are constructed from only dielectrics (figure 1 (b)). When replicated in a pseudo infinite array, both have been shown to produce perfect absorption with high quality factors in frequency space [12] [11]. These metamaterials have the advantage that they can be made subwavelength allowing for highly efficient absorption and can be tuned to work across a large range of frequencies. In particular, the all-dielectric approach yields advantages over the hybrid structures as the conducting components yield low melting point and high thermal conductivity compared to dielectrics. Here we present and analyse all-dielectric unit cell structures with high degrees of symmetry and study their absorbance across different incident angles for *S* polarized radiation in the terahertz domain. Due to their high absorbance across many different angles these unit cell designs have applications in sensing equipment and energy harvesting, particularly where high incident angles may occur.

In this report, we simulate an electromagnetic plane wave impinging on an array of absorbers. These absorbers generate a scattered field which interacts with the impinging plane wave. The properties of the scattered field are altered through changing the array geometry, producing destructive interference in the forward propagation direction.

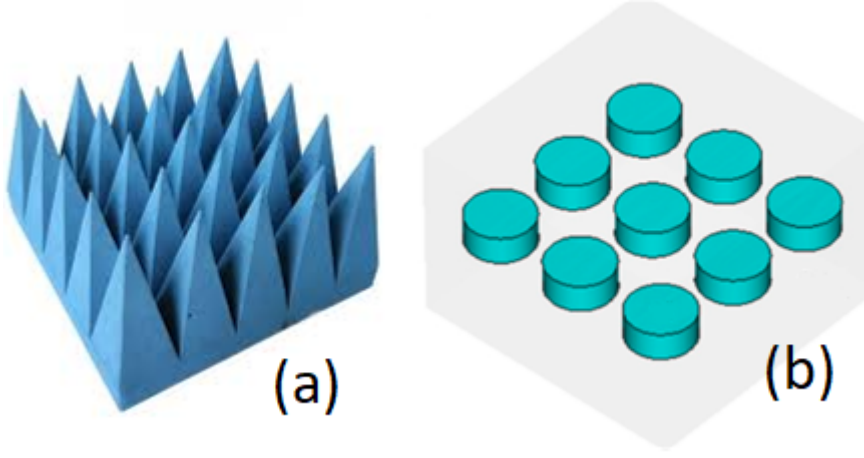


Figure 1: Electromagnetic broadband absorber [1] (a) and dielectric disk resonant absorber [15] (b).

Background Theory

Mechanical Oscillators

One of the simplest cases of a resonator is a mass m confined to move only in the horizontal direction attached to a spring of constant k and damper of rate c , whose other ends are attached to an immovable object. We use a co-ordinate system centered at the equilibrium position of the mass and define x as the distance the mass is away from the equilibrium position. We then introduce an external driving force $F(t) = F_0 \cos(\omega t)$ that acts on mass. By Newton's 2nd law and Hooke's law we get the equation:

$$m \frac{d^2x}{dt^2} + c \frac{dx}{dt} + kx = F_0 \cos(\omega t) \quad (1)$$

We can solve this differential equation by trying a solution $x(t) = Ae^{i\omega t}$ in equation 1:

$$\frac{d^2x}{dt^2} + \gamma \frac{dx}{dt} + x\omega_0^2 = \frac{F_0}{m} e^{i\omega t}, \quad (2)$$

where $\gamma = \frac{c}{m}$ and $\omega_0^2 = \frac{k}{m}$. This can be solved to give the real amplitude A

$$A = \frac{F_0}{m} \frac{1}{\sqrt{(\omega_0^2 - \omega^2)^2 + \omega^2\gamma^2}} \quad (3)$$

By plotting (see figure 2) the steady-state amplitude of oscillation as a function of ω for constant parameters k , m , F_0 and c we see that our amplitude is maximal at some frequency ω_{max} , which we call the resonant frequency. In this specific case there is only one such frequency. However

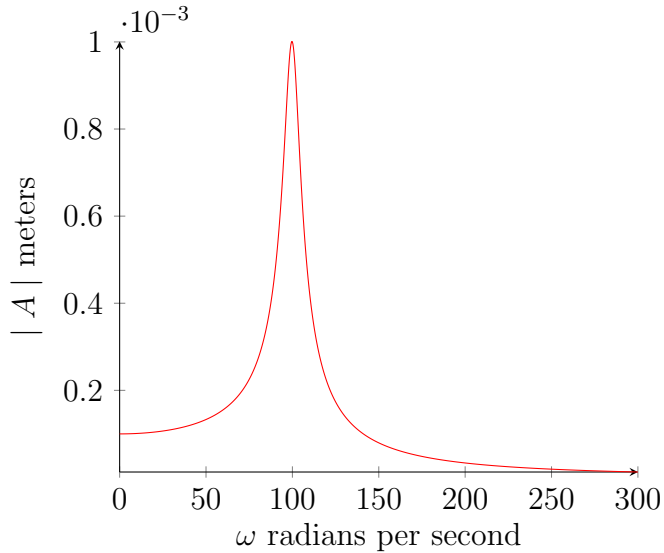


Figure 2: Steady state oscillation amplitude as a function of driving force frequency with $\gamma = 10$, $m = 1Kg$, $F_0 = 1N$ and $\omega_0 = 100Rads^{-1}$.

in general for a discrete oscillator with N degrees of freedom there may exist N resonant frequencies [7] [8]. By solving for ω to maximise the amplitude we find ω_{max} to be:

$$\omega_{max} = \sqrt{1 - \frac{Q^2}{2}}\omega_0, \quad (4)$$

where Q is the quality factor, $\frac{\gamma}{\omega_0}$. Here we interpret the quality factor to be a measure of the number of cycles the oscillator will undergo from resonance without the application of the driver. However, it can also be interpreted as a measure of the width of the peak about which the resonance occurs [7] [8]. By substituting equation 4, into equation 3 we get equation 5.

$$A_{max} = \frac{F_0}{k} \frac{Q}{\sqrt{1 - \frac{1}{4Q^2}}} \quad (5)$$

Thus the maximum response from the discrete oscillator is inversely proportional to the spring constant and approximately proportional to the quality factor for $Q > 1$.

Lorentz Oscillator

However, these discrete oscillator models are not limited to mechanical systems and can be used to model the properties of dielectrics. The Lorentz electron model imagines the atom being comprised of a single electron of mass m and charge q attached to a spring of constant k whose end is fixed to the nucleus, which due to its large mass is considered fixed. We also consider some damping rate, c , which originates from radiation damping [8]. If we consider an external field $E(t)$ pointing along the length of the spring, then by a similar method to that of the mechanical oscillator we arrive at equation 6

$$m \frac{d^2x}{dt^2} + c \frac{dx}{dt} + kx = qE(t) \cos(\omega t), \quad (6)$$

where x is the direction along the length of the spring from the nucleus to the electron. By using two definitions of electric polarization, given by equations 7 and 9.

$$\vec{P} = -Nq\vec{x}, \quad (7)$$

where P is the polarization, \vec{x} the displacement from the nucleus to the electron, q the elementary charge and N the number of such dipoles in the volume. With equation 7, equation 6 can be rearranged to give equation 8 [9]

$$\frac{d^2P}{dt^2} + \gamma \frac{dP}{dt} + \omega_0^2 P = \frac{Nq^2}{m} E(t), \quad (8)$$

where $\gamma = \frac{c}{m}$ and $\omega_0^2 = \frac{k}{m}$. We introduce a second definition

$$\vec{P} = \epsilon_0 \xi_e \vec{E}, \quad (9)$$

where ϵ_0 is the permittivity of free space and χ_e the electric susceptibility of the material. With equation 9, we can solve equation 8 for P [9] and then rearrange to give the relative permittivity ϵ_r of the material [8],

$$\epsilon_r = 1 + \frac{Nq^2}{m\epsilon_0((\omega_0^2 - \omega^2) + i\omega\gamma)}. \quad (10)$$

Polarizations

In our case we are dealing with electromagnetic waves. These waves may have complex polarizations, but here we will deal only with their linearly polarized variants, P and S polarizations. We consider a flat infinitely symmetric surface on the x y plane onto which our electromagnetic wave impinges with wavevector \vec{k} with some polar angle θ and azimuthal angle ϕ as shown in figure 3. By considering the reflected wavevector \vec{k}' , we uniquely define a plane in which \vec{k} and \vec{k}' lie. The P polarization is then defined when the electric field varies parallel to the plane and the S polarization when the electric field varies perpendicular to the plane. By linear combination of these two S and P polarizations all other linearly polarized electromagnetic waves with wavevector \vec{k} can be constructed. In the special case that θ and θ' are both zero, the plane defined by \vec{k} and \vec{k}' becomes a line making the S and P polarizations equivalent [5]

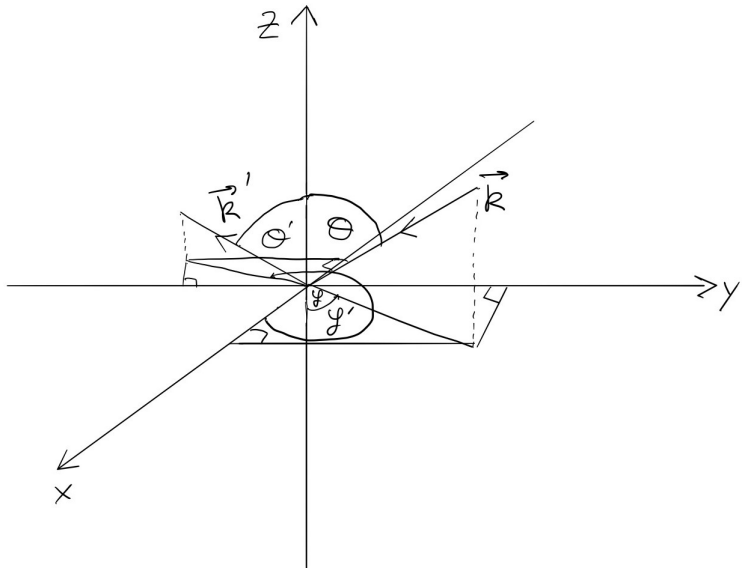


Figure 3: Diagram of wave of wavevector \vec{k} , polar angle θ and azimuthal angle ϕ being reflected from the x - y plane producing a reflected wave of wavevector \vec{k}' with polar angle θ' and azimuthal angle ϕ' forming a plane between them.

Mie Resonances

When an electromagnetic plane wave interacts with a dielectric body, it may excite electric and magnetic resonances. These Mie resonances approximate resonating electric and magnetic multipoles whose resonant frequencies depend on the dielectric constant and geometry of the body. Thus, by changing the geometry of the body, the resonant frequency of an electric and magnetic resonance have been shown to be able to coincide in many shapes such as cylinders [12] [6]. These electric and magnetic multipole resonances produce their own scattering field which interfere with the incoming wave [10]. By tuning the geometry and thus overlapping these electric and magnetic resonances it has been shown that arrays of simple shapes such as cylinders can be made perfectly absorbent in the terahertz regime [12].

Diffraction and Interference

In an array of resonators there are several complications to this. The first is diffractive effects, which bound the scale of the unit cells perpendicular to the incident wave. An approximate analysis of this effect is as follows. To analyse our array we consider each resonator as a point and flatten our 2D array into a 1D array with period p . We then analyse our 1D array as a diffraction grating with plane wave incident at angle θ_1 from the normal. We then consider two rays of light emanating from the periodic structure at angle θ_2 as seen in figure 4.

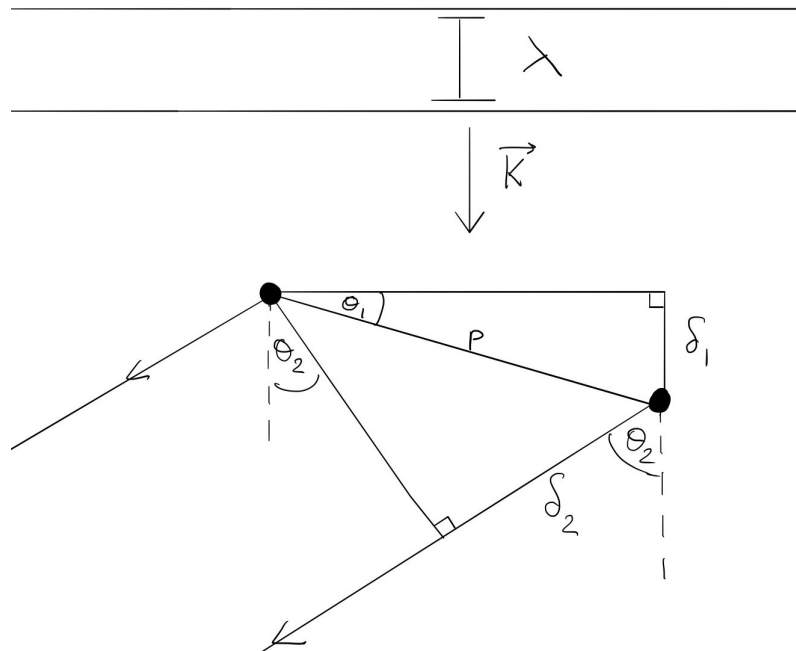


Figure 4: Diffraction diagram with plane wave of wavevector k , wavelength λ incident on diffraction grating of period p , θ_1 the angle between the normal of the periodic structure and incident wavevector \vec{k} , θ_2 the ray angle deviation from \vec{k} after interacting with the array and δ_1 and δ_2 path length differences between the left and right rays.

The path length difference which we call δ_1 resulting from the difference in distance in reaching two adjacent elements is then,

$$\delta_1 = p \sin(\theta_1). \quad (11)$$

There are now two directions that θ_2 could take, partially negating the path length difference and adding two it. We analyse the latter to give a lower bound on the conditions for p , θ_1 and θ_2 giving equation 12

$$\delta_2 = p \sin(\theta_2 - \theta_1), \quad (12)$$

making the total path length difference $p | (\sin(\theta_1) + \sin(\theta_2 - \theta_1)) |$. When such a path length difference is a multiple of the incoming wavelength λ , constructive interference occurs giving equation 13

$$m \frac{\lambda}{p} = \sin(\theta_1) + \sin(\theta_2 - \theta_1), \quad (13)$$

where m is a non zero positive integer.

Therefore, for a given θ_1 , there exists no θ_2 and m such that equation 13 is satisfied, no diffraction will occur. At normal incidence, $\theta_1 = 0$, the diffraction condition is

$$m \frac{\lambda}{p} = \sin(\theta_2) \quad (14)$$

By taking our wavelength λ to be greater than some $\lambda_0 > p$, the term $m \frac{\lambda}{p} > 1$ and thus, there doesn't exist a real θ_2 such that the diffraction condition can be met, eliminating the possibility of diffraction occurring in our 2D array at normal incidence.

For our purposes however we also consider azimuthal angle variance, which for our 2D array changes the period p to some p' by equation 15 as shown in figure 5

$$p' = \frac{p}{\cos(\phi)}, \quad (15)$$

where ϕ is the azimuthal angle.

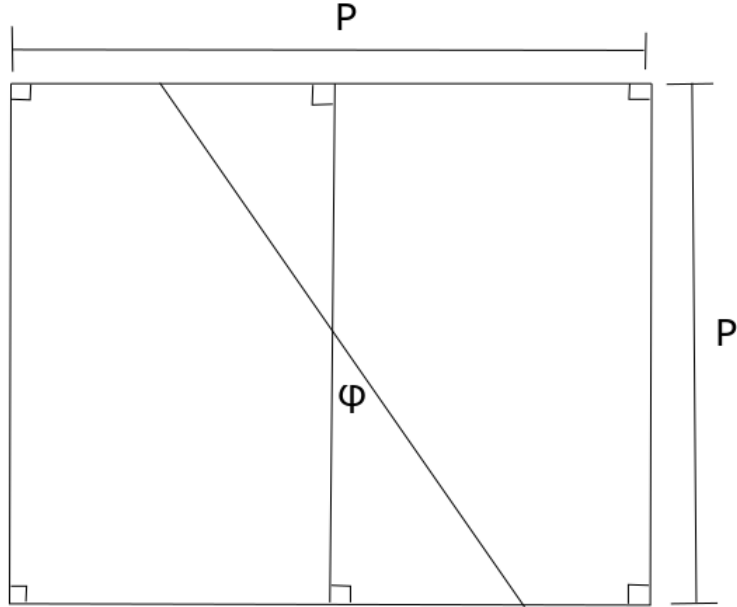


Figure 5: Top down view of unit cell showing approximate period changing as azimuthal angle ϕ varies.

To get a lower bound on the normal polar θ_1 and azimuthal ϕ angles for diffraction we take the worst case, where $\theta_2 = 90$ degrees and λ is a minimum, giving a diffraction condition of

$$m \frac{\lambda}{p} \cos(\phi) = \sin(\theta_1) + \cos(\theta_1). \quad (16)$$

Thus, for polar and azimuthal incident angles θ_1 and ϕ that satisfy equation 16 we should see no diffraction.

$$\frac{\lambda}{p} \cos(\phi) > \sin(\theta_1) + \cos(\theta_1) \quad (17)$$

The second, perhaps more complicated interaction is the interference between elements of the array. In the case that the resonators are a large distance away from each other, the resonators become uncoupled and so act independently. However, in the case where these dielectric resonators become closer to each other, such a model quickly diverges from reality. As this is not the topic of the report however this will not be covered, but is of interest in future.

Simulation Software

To design, simulate, gather data and optimize our absorber unit cell designs *CST Microwave Studio* was used. For the purposes of this report, the simulation software was used in the frequency domain to simulate the transmission, reflection and absorption of meta material structures as a function of incident electromagnetic plane wave frequency. To simulate the periodic 2D infinite array of structures, CST's unit cell boundary conditions were used in the directions perpendicular to the arrays' surface normal. To simulate the interactions between the electromagnetic plane wave and a unit cell, CST uses a meshing system. In this, the program divides the simulation space into finite cells via one of the selected algorithms, which in this case was the default tetrahedral mesh. It then solves Maxwell's equations. The length scale of this meshing can be adjusted, producing a better approximation.

To interact with the simulation space, CST uses ports, which can be used to generate electromagnetic excitations and measure them. Before simulating, the user must define the ports' location in the simulation space and which ports will produce an excitation. When simulating, the program computes the scattering parameters of the system decomposed into a set of modes for each port. For example, suppose we are only considering the first mode and that we have port 1 defined to the left of a body and port 2 to the right and we excite port 1 as shown in figure 6.

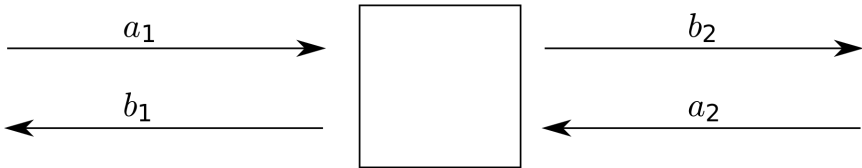


Figure 6: Simplified model of S parameter use, with port 1 defined to the left, port 2 to the right and interacting body in the center [4]

Here we define a_1 and a_2 to be the incident power wave generated by ports 1 and 2 respectively and b_1 and b_2 to be the received power wave at port 1 and 2 respectively by the first mode. The four S parameters related to the system are defined as, $S_{11} = \frac{b_1}{a_1}$, $S_{21} = \frac{b_2}{a_1}$, $S_{12} = \frac{b_1}{a_2}$ and $S_{22} = \frac{b_2}{a_2}$ [4]. Using these S parameters, reflection, transmission and absorption coefficients can then be defined across the frequency spectrum. A second method for output in CST, called the field monitor is also used. In the case of the frequency domain, these monitors cover the entire simulation space at a specific frequency and can measure the magnetic and electric field strength and direction. To refine structural parameters, CST uses an optimizer function which allows the user to set goals such as maximise the maximum of a function of S parameters. The program defines a goal function for each goal which is minimised when the goal is achieved. The optimizer then adjusts user specified parameters within a specific range to find a minimum to the goal function.

Absorber Parameterisation

In the proposed unit cell designs, the array of absorbers is set to lie in the x - y plane, with the substrate extending symmetrically in the $+z$ and $-z$ directions, with a high index structure being embedded in the substrate. The electromagnetic plane wave is simulated as propagating from above the array in the $+z$ region to below the array in the $-z$ region. In addition, to mitigate near field interference the two ports, “port max” and “port min” were placed at the largest simulated wavelength above ($z \geq 0$) and below ($z \leq 0$) the array. Throughout absorber design, the material parameters were fixed at the values given in table 7.

Object	Relative Permittivity	Dielectric loss tangent
Main structure	7.405	0.032
Substrate	2.09	0.007

Figure 7: Dielectric material properties of the main structure and substrate common to all absorber designs. With all other properties that of a vacuum. Constants used are invariable in incident frequency.

Substrate Parameterisation

The substrate used material parameters described in table 7. For each unit cell the substrate consisted of a solid prism with two parameterisations. The first was the thickness in the x and y directions denoted T , which extends in the x and y directions from the high index structure. The second was the upper thickness denoted UT which extended similarly in the two z directions as shown in figure 8 for the cylinder high index structure.

Cylinder

The first unit cell design is a high index dielectric cylinder (figure 9), used to replicate results from [12]. The cylinder is orientated in the $\pm z$ direction and parameterised by height (H), radius (R) and the z position ($zPos$) of the center of the cylinder.

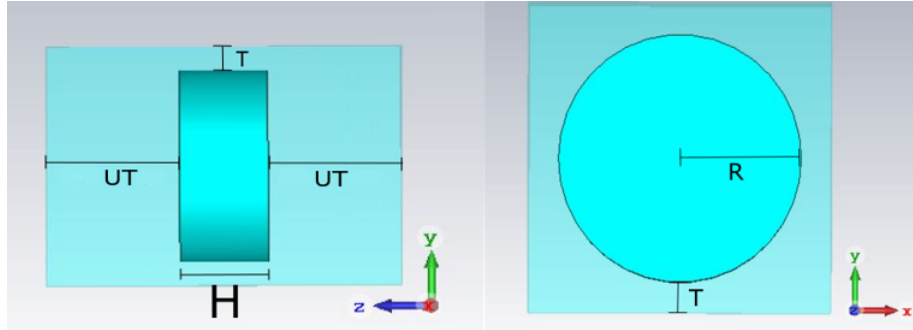


Figure 8: Side (left) and face on (right) diagram of parameterization of cylinder-substrate unit cell with x and z axis pointing out of the page respectively. Darker blue opaque material is high index cylinder, light blue translucent material is low index substrate.

Three Intersecting Cylinders

The second unit cell design is three of the basic cylinder structures with flat faces in the x , y and z directions, intersected at each other's centers as seen in figure 9. The same parameters, height (H), radius (R) and z position ($zPos$) is common to all cylinders. The idea for constructing the 3 cylinder shape was to combine the low incident angle performance of each of the three perpendicular cylinders giving good absorbance across a wider range of angles.

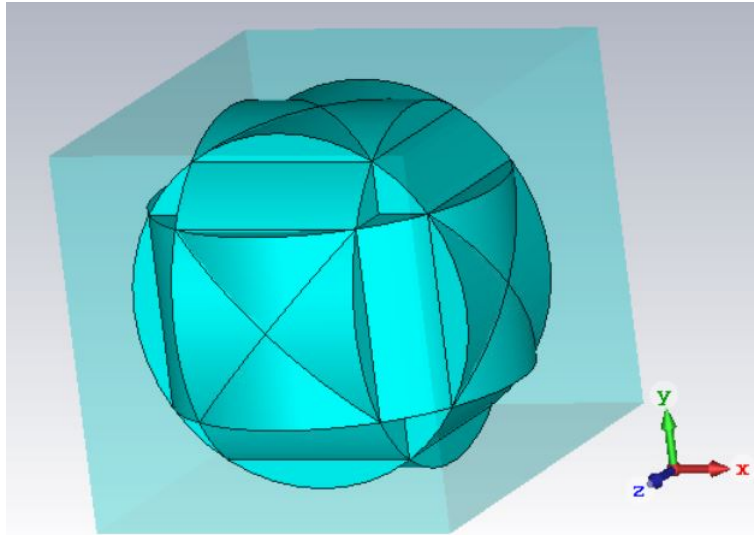


Figure 9: Diagram of unit cell structure of three high index intersecting cylinders (opaque blue) embedded in low index substrate (translucent blue).

Dimpled Sphere

As an approximation to the three intersecting cylinders, an 8 dimpled sphere absorber was simulated (figure 10). The dimpled sphere absorber consisted of a main sphere, of radius $MRadius$ with a z direction shift of $zPos$. To generate the dimples, spheres of radius $ORadius$ with 8 positions described by $(\pm \frac{ODistance}{\sqrt{3}}, \pm \frac{ODistance}{\sqrt{3}}, \pm \frac{ODistance}{\sqrt{3}} + zpos)$ were used to cut away the main sphere. The created dimples were filled with substrate material.

Optimization

To optimize each absorber type, the plot of absorbance as a function of frequency was considered, such as fig 12 at normal incidence. The optimizer was then run to produce as high an absorption peak as possible within the frequency domain 0.5 – 1.2 THz. This frequency range produced a free space wavelength between $250\mu m$ and $600\mu m$, which by the normal diffraction equation 14 gives a maximum bound on the unit cell size of $250\mu m$ at normal incidence. However, as we are investigating our array structure over various azimuthal and polar incidence angles, it was decided that a bound of $200\mu m$ on the period should be used, as this allowed for a region of azimuthal and polar angles that do not yield diffraction. The unit cell height was also bounded by $250\mu m$ so as to limit the array to subwavelength thickness.

During optimization, the periodicity and height bound was enforced differently between the two shapes, with the details in the appendix figures 31 and 32.

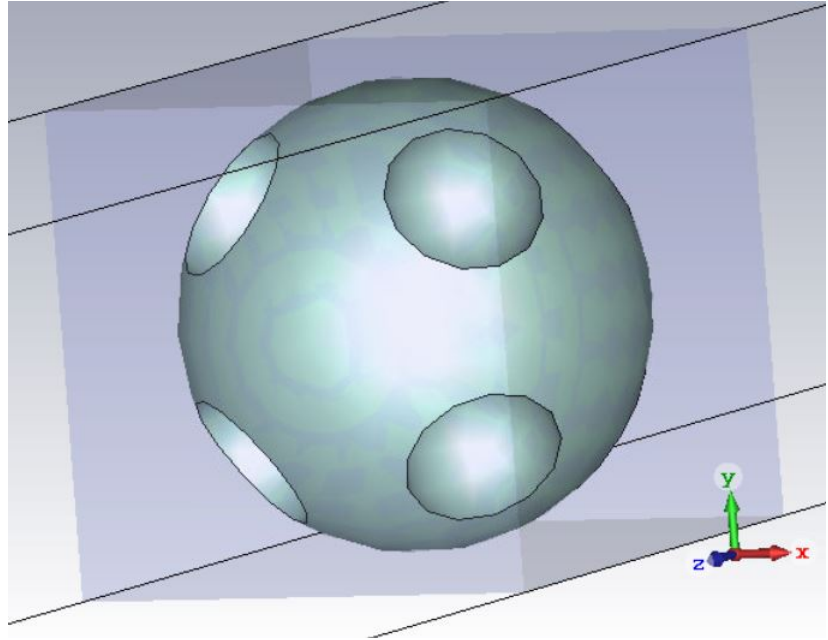


Figure 10: Unit cell structure of high index 8 dimpled sphere (opaque silver) embedded in low index substrate (translucent purple).

For optimization of all bodies, port max was excited at normal incidence with an S polarized plane wave. The scattering parameters S_{max_i,max_1} and S_{min_i,max_1} for the first five modes and their orthogonality were used to calculate the absorption coefficient in equation 18:

$$A(f) = 1 - \sum_{i=1}^5 ((S_{max_i,max_1} S_{max_i,max_1}^*) + (S_{min_i,max_1} S_{min_i,max_1}^*)), \quad (18)$$

where f is frequency in Hertz, A the absorption coefficient, $*$ denotes the complex conjugate and the index i denotes the i th mode. The first five of these modes were used as it was found that higher order modes contributed negligibly to the signal. A template goal called Global y-Maximum was then applied to the absorption coefficient with target value 1. We mention this technical detail in the interest of result replication. When run, this optimized over the selected parameters to minimise the smallest distance between a value of 1 and the absorption coefficient across the frequency range. Initially, the trust region algorithm was used in optimization. However it was found that this algorithm was not suitable for the large number of parameters and large search space. In its place, the genetic search algorithm was used.

Angle Sweep

To measure the frequency absorption spectra over changing incident angles, the azimuthal and polar angles of the waves k vector were defined as follows. In all cases the array structure sat parallel to the x - y plane, with the high index inner structure having lines of symmetry along the x , y and z directions. The polar angle θ was then defined as the acute angle between the z axis pointing out of the array and the wavevector k . The azimuthal angle was defined as being the angle the k vectors projection into the x - y plane made with the x axis.

To measure the frequency absorption spectra over changing incident angles, the azimuthal and polar angles of the plane waves k vector were varied. Due to the x and y directions being lines of symmetry, azimuthal variations of 0 to 45 degrees captured all azimuthal dependence. To simulate the S polarization, the excitation ports mode was set to $TE(0,0)$, which produced a mathematically infinite S polarized infinite plane wave for the array to interact with.

Results and Analysis

Cylinder

Normal Incidence Absorption and Resonances

The cylinders design was used as a stepping stone to more complex shapes, having already been simulated at normal incident angles in reference [12]. The cylinder's parameters shown in figure 11, were copied and converted into our parameterisation from reference [12] and the absorption coefficient calculated via equation 18 which gave a peak absorption of 99.48% at a frequency 1.007 Thz as shown in figure 12, closely agreeing with previous work [12].

Measurement	value (μm)
T	17.25
UT	91.33
H	60.03
R	69.25

Figure 11: Cylinder unit cell geometry parameters

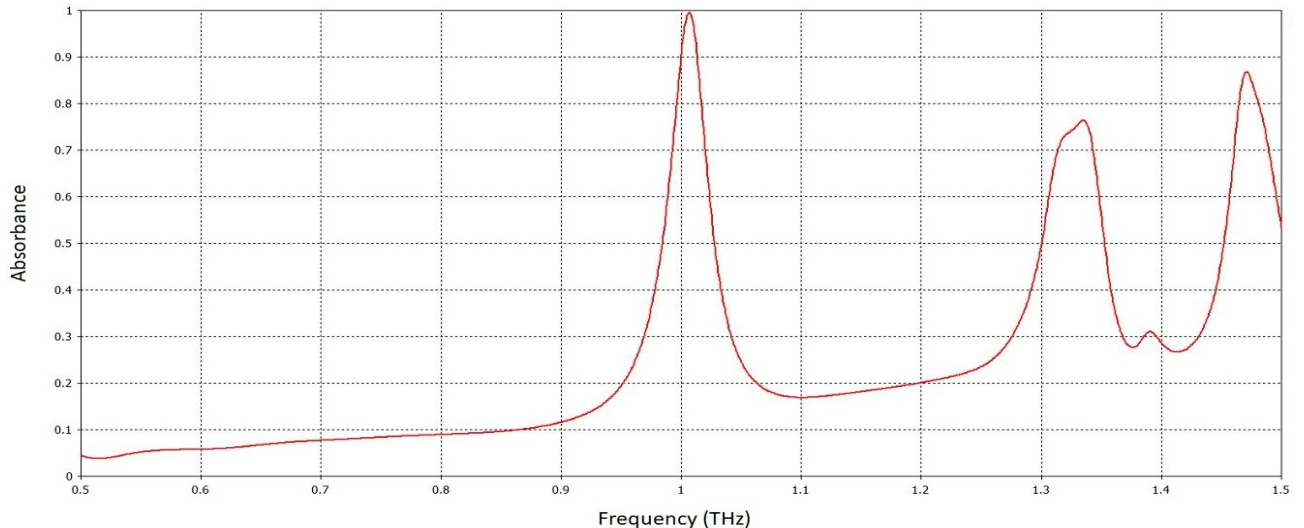


Figure 12: Absorption spectrum over frequency range 0.5 to 1.2 THz for high index cylinder unit cell design with parameters given in figure 11

When the radius is perturbed, we see separation of the main absorption peak at 1.007 Thz, forming two absorption peaks denoted 1 and 2 at 0.751 and 0.801 terahertz respectively as seen in figure 13.

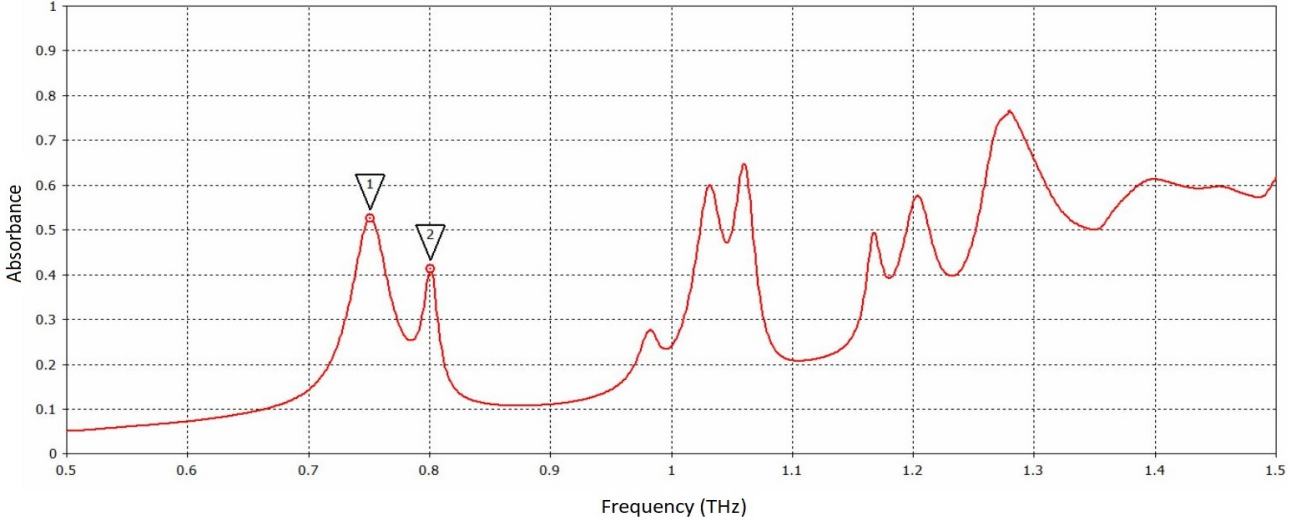


Figure 13: Absorption frequency spectrum for cylinder unit cell design with parameters in figure 11 and radius perturbed to $100\mu\text{m}$. Pointers 1 and 2 indicate peaks at 0.751 and 0.801 THz where electric and magnetic field monitors are placed.

Field monitors for both electric and magnetic fields were placed at frequencies 0.751 THz and 0.801 THz producing the approximate electric and magnetic dipole resonances seen in figure 14 respectively, replicating the results of [12] and showing the absorption peak at 1.007 THz in figure 13 to be the superposition of electric and magnetic dipole resonances.

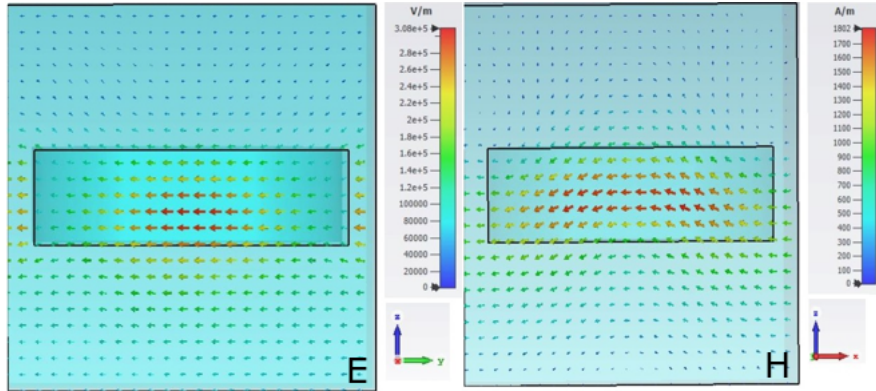


Figure 14: Electric (left) and magnetic (right) fields within dielectric cylinder unit cell with radius perturbed to $100\mu\text{m}$ at frequencies of 0.751 and 0.801 THz respectively

Cylinder non-normal Incidence Absorption and Resonances

We now move on from normal incidence to study angular variation, with exact definitions of angles given in section *Angle Sweep*. We already know that the peak absorption at normal incidence is 99.5 %. How does this change for non-normal incidence? This is shown in figure 15. For incidence angles $\theta > 5$ and $\phi > 5$ degrees, the peak absorbance is no greater than 64.5 %. In general, we see that as the polar and azimuthal angles increase, the absorbance decreases. However, there are some exceptions, notably the region $0 \leq \theta \leq 5$, $0 \leq \phi \leq 45$ degrees and $35 \leq \theta \leq 40$, $0 \leq \phi \leq 5$. In the first case, due to the small angle polar angle θ , the incident electromagnetic wave is approximately normal regardless of ϕ . To analyse the second, we fix $\theta = 35$ degrees and plot the absorption peaks for $\phi = 0, 5, 10$ degrees, giving figure 16.

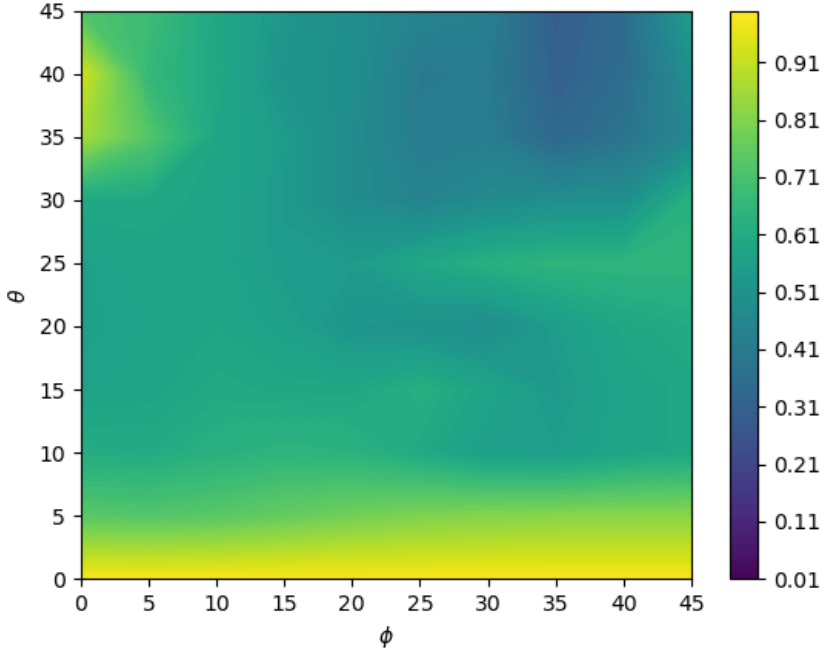


Figure 15: Maximum Absorbance of cylinder design array over frequency 0.907 to 1.107 THz with parameters given in figure 11 for S polarized incident electromagnetic radiation at 100 samples of azimuthal angle ϕ and polar angle θ with 5 degree inciments in both.

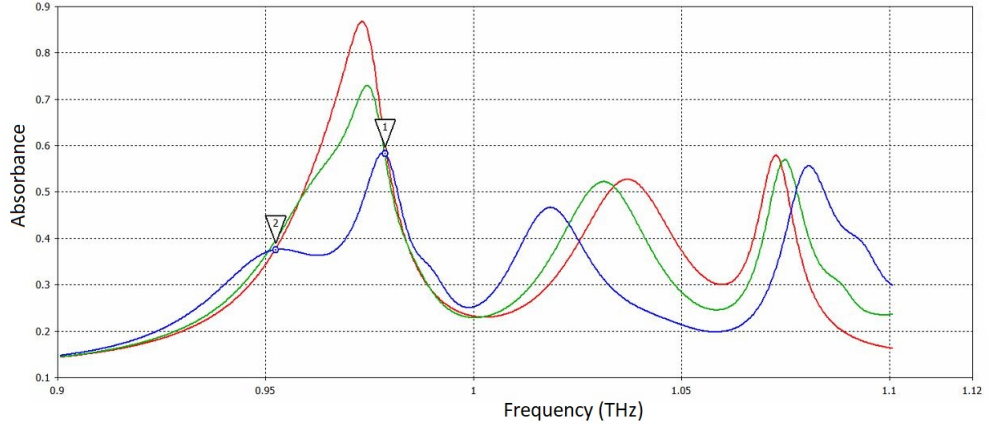


Figure 16: Absorption spectrum for optimized cylinder unit cell design over frequency of 0.907 to 1.107 Thz for incidence angles of $\theta = 35$ and $\phi = 0$ (Red), $\phi = 5$ (Green) and $\phi = 10$ (Blue), with markers 1 and 2 indicating peaks in the $\theta = 35$, $\phi = 10$ at 0.97977 and 0.95247 Thz respectively.

With $\theta = 35$ and $\phi = 10$ degrees, both electric and magnetic field monitors were placed at each of the frequencies 0.97977 and 0.95247 THz, producing the magnetic and electric fields shown in 19. Although these resonances are quite complicated, we see that in all of them adjacent unit cells have different fields in all cases, either in direction or magnitude. This is most likely due to the path length distance generated by the incident wave reaching each absorber at different times, denoted δ_1 in figure 4. In addition, in each panel, one approximate electric or magnetic resonance can be seen. For example, in the top two panels representing a frequency of 0.95247

THz, there exists an approximate magnetic dipole resonance in the right absorber and an approximate electric dipole resonance in the second panel left absorber. However the top panel left and second top panel right absorber appear to have a more complicated field structure. In the case of the bottom two panels however only the second from bottom left absorber shows an approximate magnetic dipole resonance and the others have no obvious discernible pattern.

3 Crossing Cylinders and The 8 Dimpled Sphere

Crossing Cylinders Normal Incidence Absorption and Resonance

The optimizer with genetic algorithm was run on the parameterised 3 crossing cylinder and 8 dimpled sphere unit cell structure with parameter search space given in appendix figure 31 and figure 18 respectively. We find a peak absorbance of 99.4 % and 97.9 % at 1.165 THz and 1.172 THz respectively at normal incidence.

Measurement	value (μm)
T	5.57
UT	24.74
H	97.99
R	90.14
zPos	-6.17

Figure 17: 3 crossing cylinder structure absorption optimized parameters over frequency range 0.5 – 1.2 THz at normal incidence

Measurement	value (μm)
T	1.87
UT	31.37
MR	93.33
OR	187.61
zPos	-5.53

Figure 18: 8 dimpled sphere absorption optimized parameters over frequency range 0.5 – 1.2 THz at normal incidence

In optimizing the dimpled sphere, as seen in figure 18, the radius of the central sphere (MR) plus the radius of the cutout spheres (OR) is smaller than the outer distance (OD), indicating that that the 8 dimpled sphere has been optimized to a sphere!

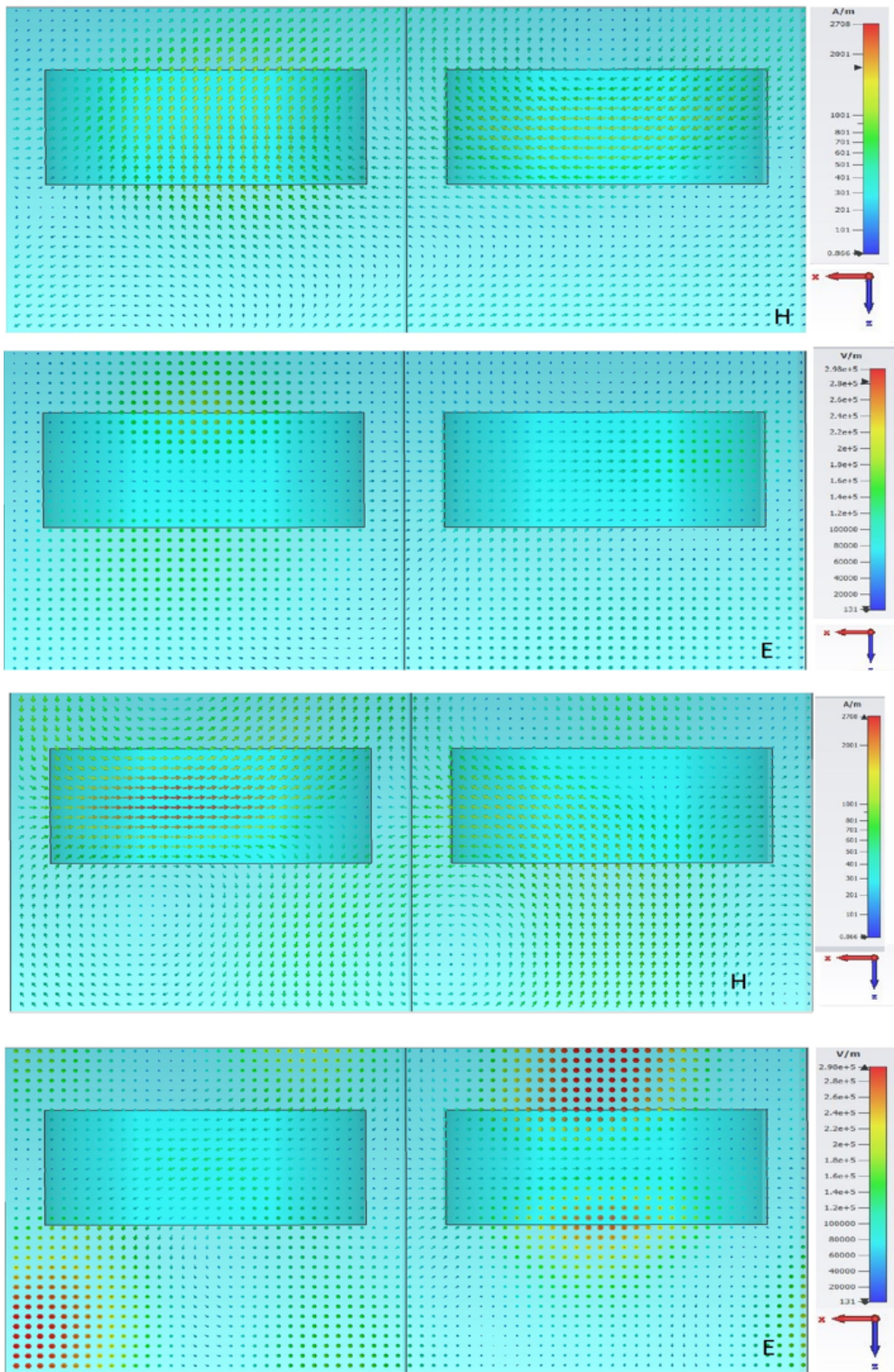


Figure 19: Magnetic and electric fields within cross-section of optimized cylinder design at phase of 0 degrees with S polarized incident light at polar and azimuthal angle $\theta = 35$ and $\phi = 10$ degrees. Top and second from top pannels are magnetic and electric field at 0.95247 Thz respectively. Second from bottom and bottom pannels are magnetic and electric fields at 0.97977 Thz respectively. Plane wave originates from bottom and travels towards the top of each panel

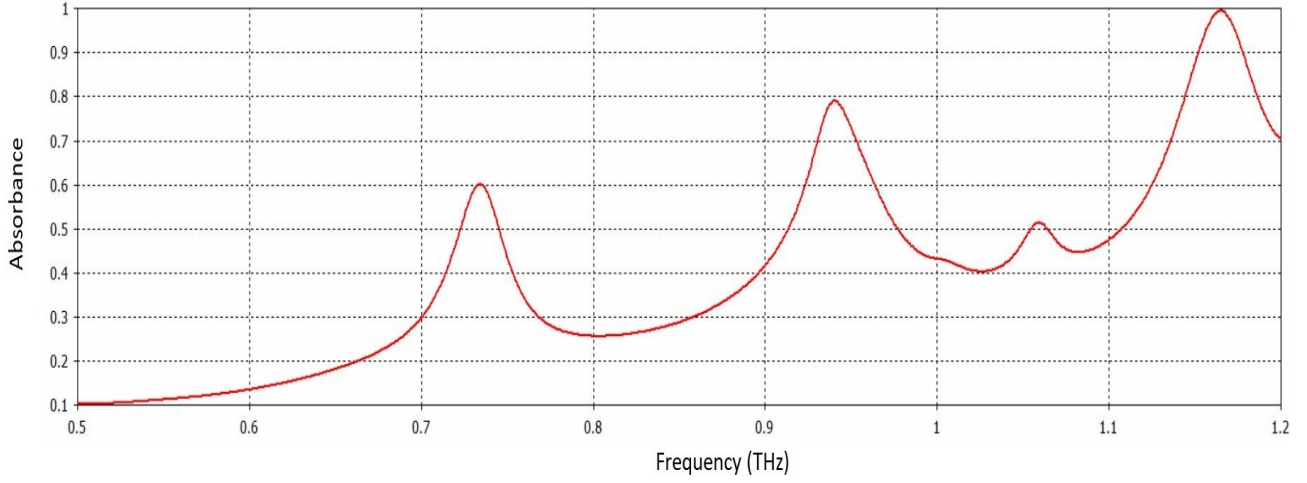


Figure 20: Frequency absorbance spectrum of high index 3 crossing cylinder unit cell design with optimized parameters from figure 17

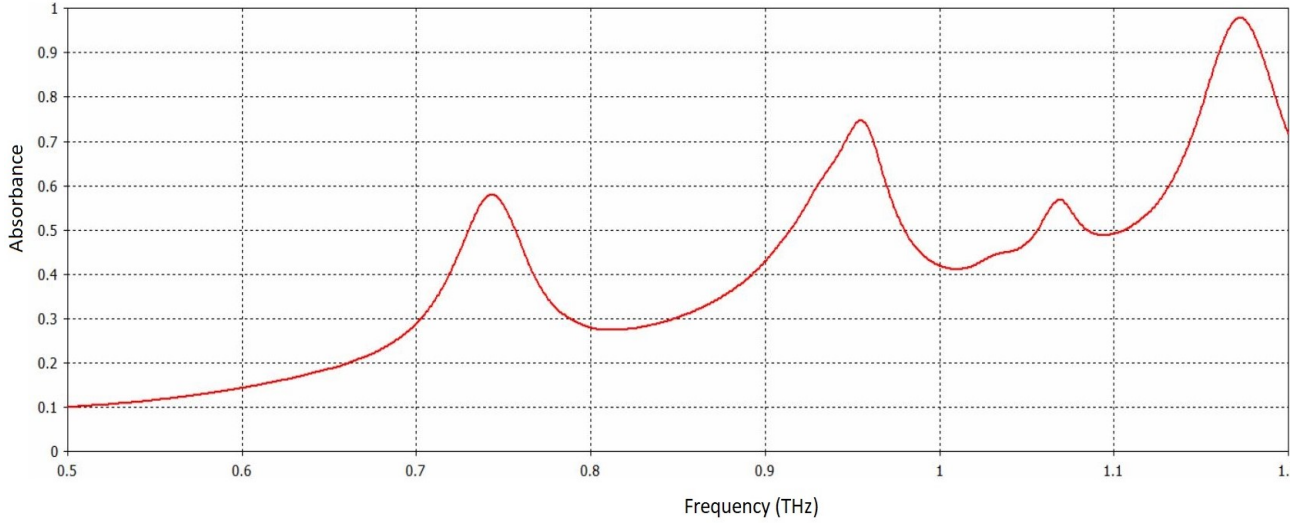


Figure 21: Frequency absorbance spectrum of high index 8 dimpled sphere unit cell design with optimized parameters from figure 18, which in this case has optimized itself to a normal sphere.

As seen in figures 20 and 21, the absorbance spectrum of the optimized 3 crossing cylinder and dimpled sphere are very similar, each with three similar magnitude, shape and location absorption peaks over the same 0.5 to 1.2 THz range. To separate the absorption peaks for the 3 cylinders and sphere unit cell design, the substrate thickness parameter T was perturbed to $25.93\mu m$, splitting the first peak of the 3 cylinders and sphere as well as the second peak of the 3 cylinders into two distinct peaks as shown in figure 22. We start by analysing the peaks of the 3 cylinders and sphere. To separate these absorption peaks located at 0.7435 THz in figure 21, perturbing the parameter T to be $25.93\mu m$ yielded two distinct peaks labelled 1 and 2 in figure 22 and a multitude of peaks higher in frequency.

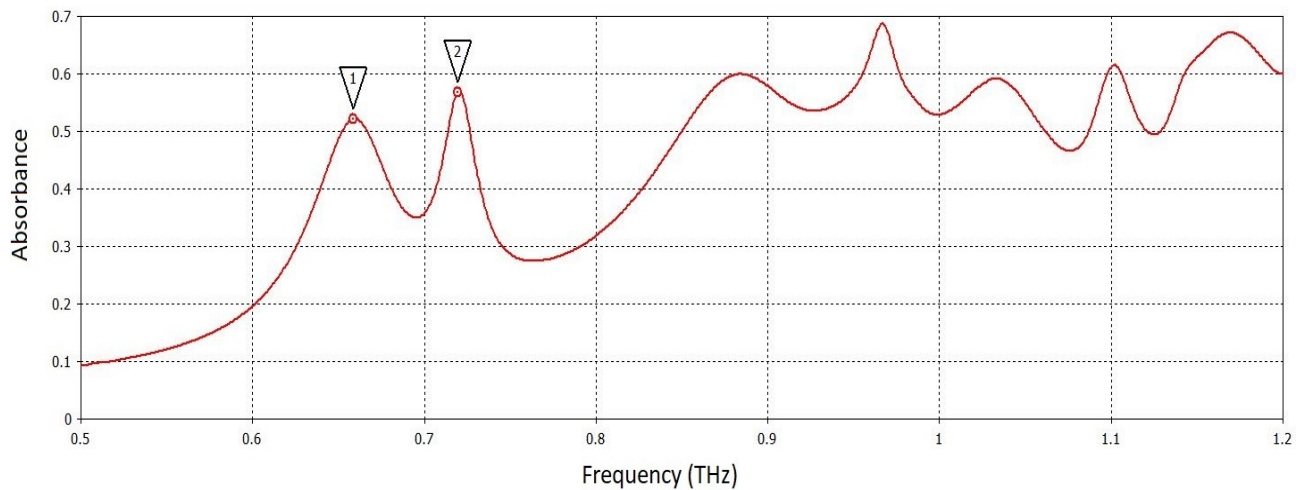


Figure 22: Absorption frequency spectrum for optimized sphere design in figure 18 with thickness (T) set to $25.93\mu m$ at normal incidence.

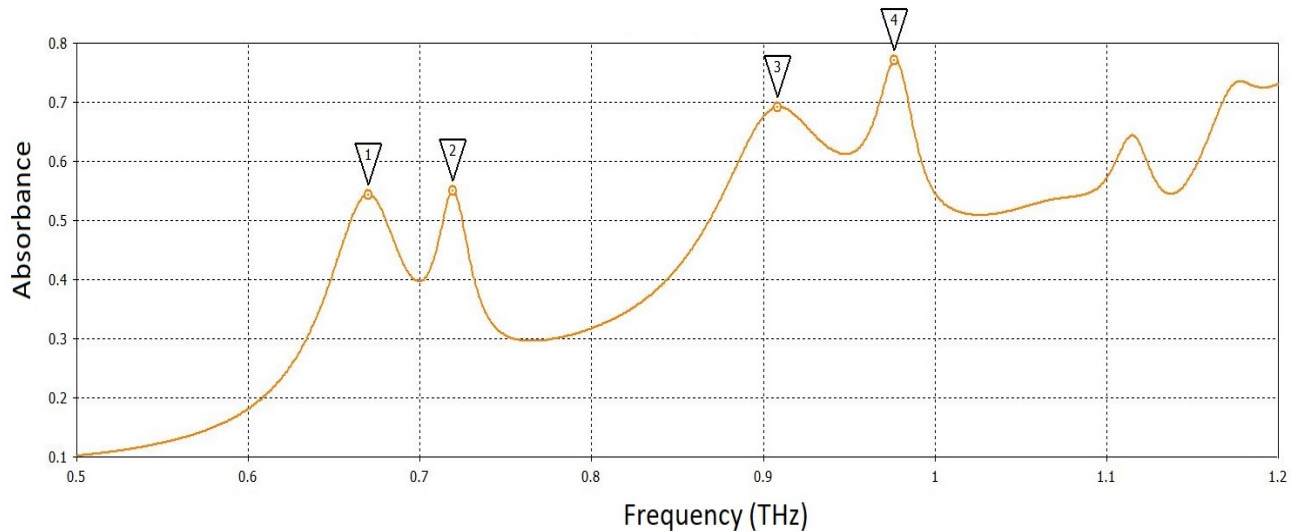


Figure 23: Absorption frequency spectrum for optimized 3 cylinder design in figure 31 with thickness (T) set to $25.93\mu m$ at normal incidence.

Electric and magnetic field monitors were then placed at peaks 1 and 2 in figure 22 and peaks 1,2,3 and 4 in 25.

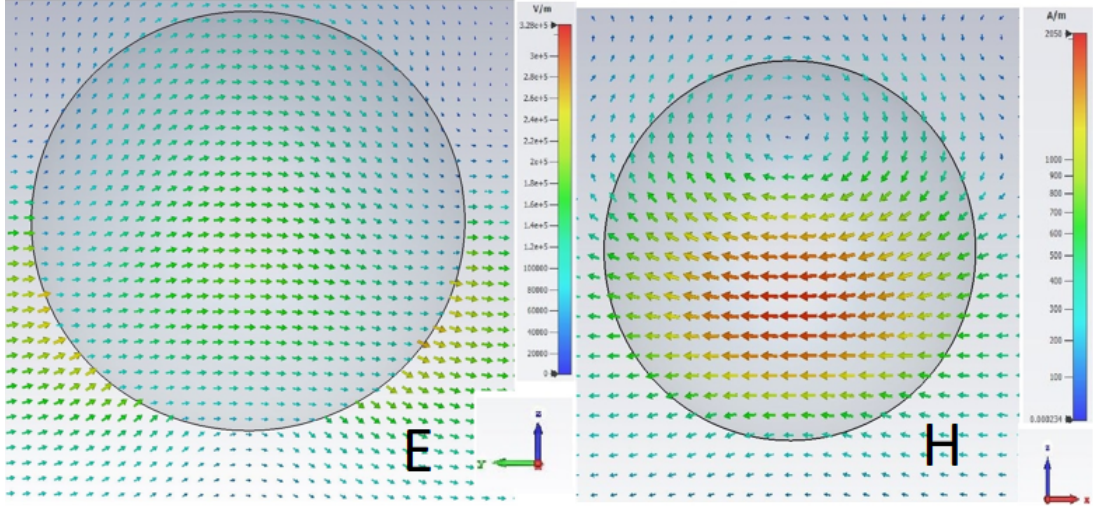


Figure 24: Electric (left) and magnetic (right) fields in cross-section of sphere unit cell design at frequencies of 0.7193 and 0.6585 THz respectively. Radiation is traveling from top to bottom in both.

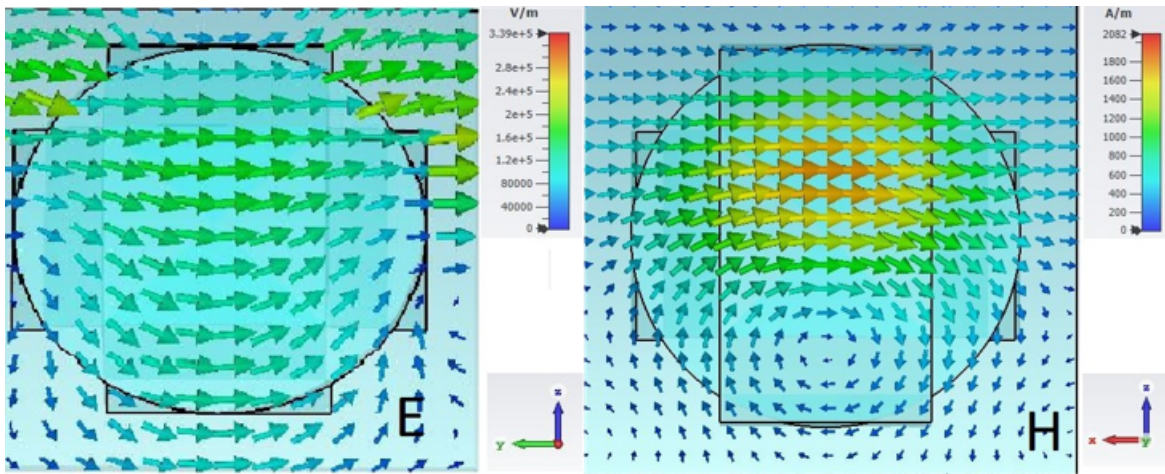


Figure 25: Electric (left) and magnetic (right) fields in cross-section of 3 cylinder design at frequencies of 0.7193 THz and 0.670 THz respectively. Radiation travelling top to bottom

Figures 24 and 25 show approximate electric and magnetic dipole resonances, showing that the lowest frequency absorption peak in the sphere and 3 cylinder is comprised of overlapping electric and magnetic dipole resonances, similar to the cylinder in figure 14.

At location 3, a clear electric quadrapole resonance can be seen, shown in figure 26. At location 4, the magnetic field pattern was a composition of a magnetic dipole resonance oscillating parallel to the magnetic field variation and a set of four rotating magnetic dipole fields, forming an magnetic octopole (figure 27). Attempts were also made to split and analyse the remaining absorption peaks by combinations of all geometric parameters. However, this approach yielded insufficient clarity and separation between split peaks making this method inadequate.

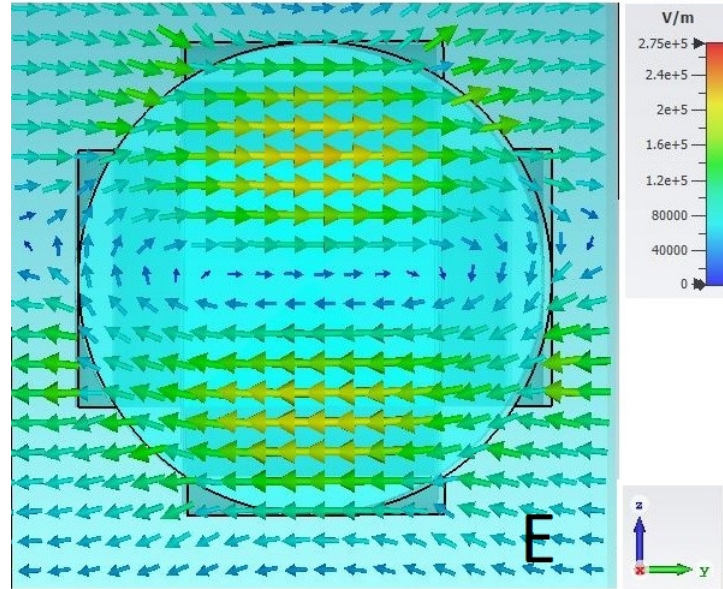


Figure 26: Electric Quadrapole resonance within cross-section of 3 cylinder design at frequency of 0.907 THz

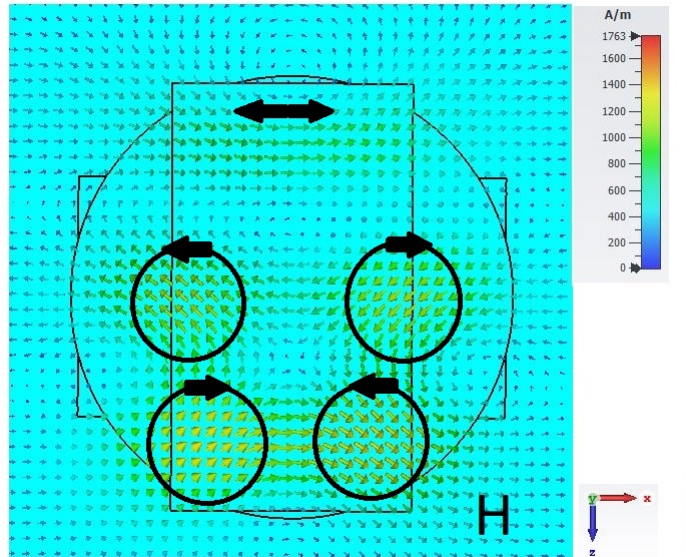


Figure 27: Magnetic field pattern within cross-section of 3 cylinder design at frequency of 0.979 THz. Black arrows indicate directions along which the magnetic field points, with circles with arrows indicating clockwise and anticlockwise turning of magnetic field vectors.

3 Cylinder and Sphere non-normal Incident Absorption

We now investigate to angular incident variation. The absorbance of the sphere and 3 cylinder structure are similar across different normal angles for S polarization, with minimum absorbance of 78.34 % and 80.99 % and maximum of 97.80 % and 99.48 %. When compared with the cylinders design, both the 3 crossing cylinder and sphere generally have higher absorbance than the cylinder past $\theta > 10$. Over $0 \leq \phi \leq 45$ and $0 \leq \theta \leq 45$ degrees, the 3 cylinder, sphere and single cylinder design yield an average absorbance of 91.32 %, 90.42 % and 62.01 % respectively.

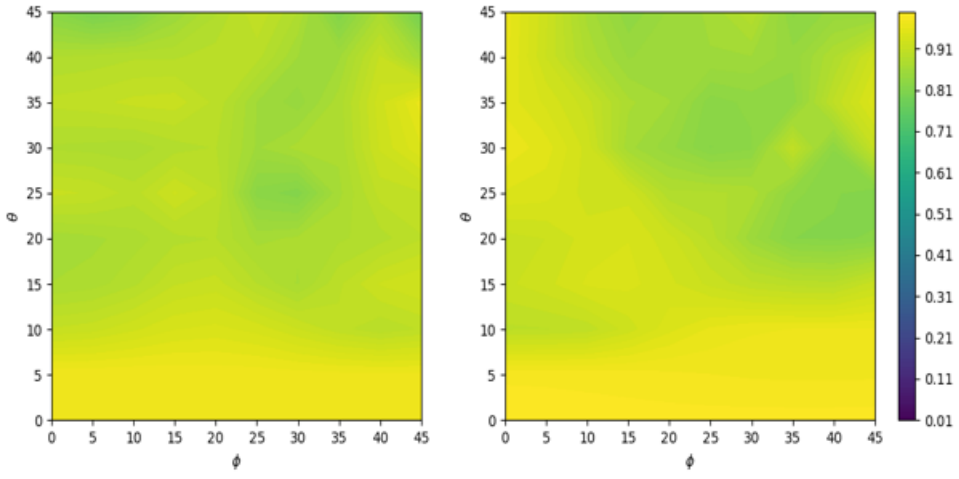


Figure 28: Maximum Absorbance of 8 dimple sphere (left) and 3 cylinder design array with over range frequency 1.072 to 1.272 and 0.907 to 1.107 THz respectively. Parameters given in figure 32 and 31. S polarized incident electromagnetic radiation was used with 100 samples of azimuthal angle ϕ and polar angle θ with 5 degree incements in both.

3 Cylinder and Sphere Tuning

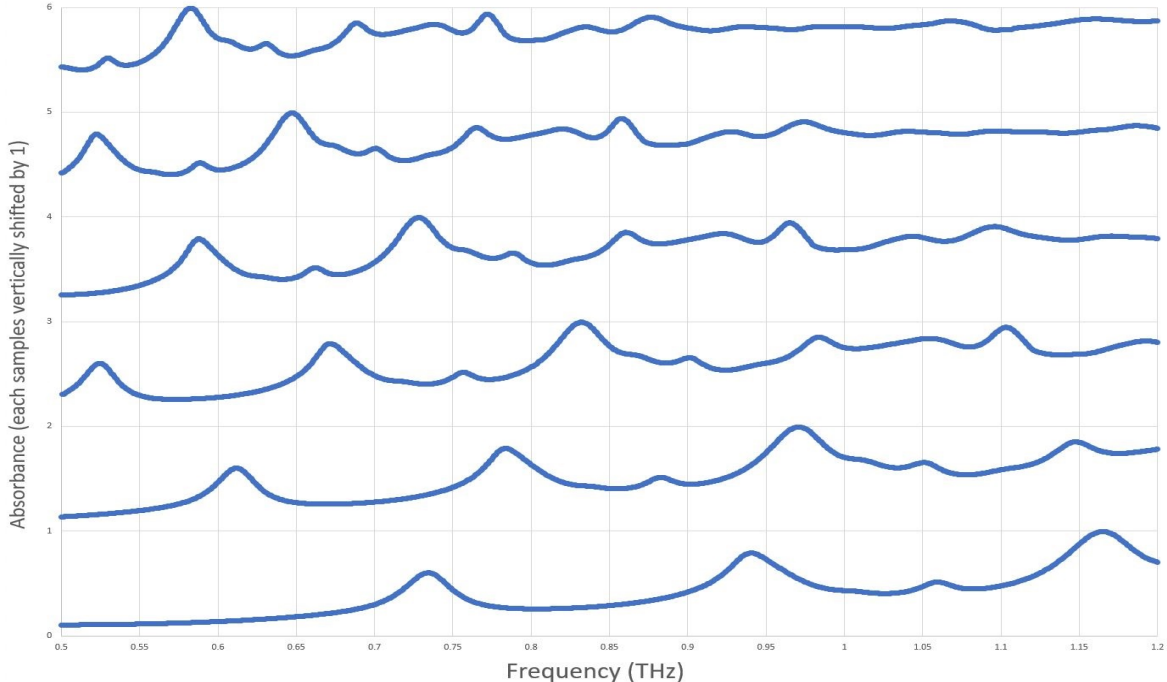


Figure 29: Absorption spectra of 3 crossing cylinders at normal incidence with all lengths multiplied by 1, 1.2, 1.4, 1.6, 1.8 and 2.0. Spectra have been vertically separated in increments of 1 with length multiplier ascending

By adding a new parameter *overallScale*, which multiplied each length parameter of each structure, the overall size of the array was increased. This resulted in absorption peaks shifting down in frequency as seen in figures 29 and 30. This was expected due to the linearity of the system and shows that the absorbance peaks frequency location can be fine tuned by

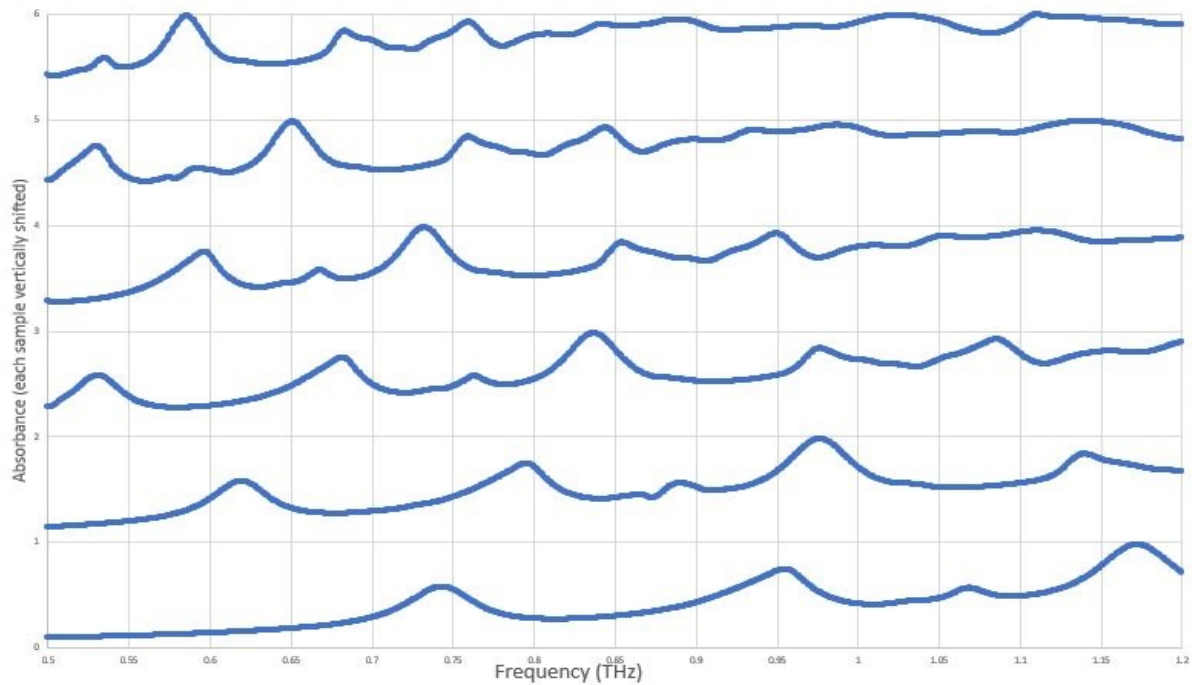


Figure 30: Absorption spectra of optimized 8 dimple design at normal incidence with all lengths multiplied by 1, 1.2, 1.4, 1.6, 1.8 and 2.0. Spectra have been vertically separated in increments of 1 with length multiplier ascending

the adjusting geometry. Further, the highest peak's magnitude is not significantly altered, maintaining a 99.4 % and 97.7 % absorbance across all length multipliers measured.

Conclusion

We have studied the absorption spectrum of a cylinder, 3 crossing cylinders and dimpled sphere unit cell designs. In each case, the designs were optimized at normal incidence giving peak absorbance of 99.5 %, 99.4 % and 97.9 % respectively. For the cylinder, the structure of the resonances was determined to be an overlap of electric and magnetic dipoles, replicating the results of [12] while the 3 cylinder and dimpled sphere designs resonances were partially determined to be a combination of higher pole electric and magnetic resonances. In all designs the absorption as a function of incident angles was determined for *S* polarized electromagnetic radiation giving average absorption of 62.01 %, 90.42 % and 91.32 % respectively over polar and azimuthal angles $0 \leq \theta \leq 45$, $0 \leq \phi \leq 45$ degrees.

The major findings here is that the 3 crossing cylinder design yields a frequency selective high absorption all dielectric structure. This structure preserves its high absorbance over a wide range of incident frequencies and can be finely tuned by adjusting the overall scale of each unit cell. This makes it a potential candidate for detectors in the terahertz domain that may experience high angles of incidence.

In future, the results for *P* polarized light at non-normal incidence should be run, giving a broader picture of the absorbers abilities. Different exact replications of real materials that can be fabricated should also be simulated and perhaps fabricated for a real world test. The nature of the higher order resonances could also be pursued by simulating arrays of electric and magnetic multipoles, providing a simplified model whose properties can be studied.

Appendix

Program accuracy configuration

All settings regarding accuracy of calculations and meshing within the program were left at default for all results presented in this report.

Optimizer Bounds

Optimizer bounds for 3 crossing cylinders

Measurement	Minimum Value (μm)	Maximum Value (μm)
Height (H)	10	200
Cylinder Radius (R)	10	100
Thickness (T)	1	$\frac{200 - \max(2R, H)}{2}$
Upper Thickness (UT)	1	$\frac{250 - \max(2R, H)}{2}$
zPos	-10	10

Figure 31: 3 crossing cylinder unit cell design parameter bounds used in optimization

Measurement	Minimum Value (μm)	Maximum Value (μm)
Main Sphere Radius (MR)	10	100
Thickness (T)	1	$100 - MR$
Upper Thickness (UT)	1	$125 - MR$
Cutout Distance (OD)	MR	$5 MR$
Cutout Radius (OR)	1	$5 MR$
zPos	-10	10

Figure 32: 8 dimpled sphere unit cell design parameter bounds used in optimization

Acknowledgements

I would like to thank Professor Ilya Shadrivov for suggesting and supervising this project.

References

- [1] Emc pioneer hybrid absorbers, <https://www.theemcshop.com/hybrid-microwave-rf-absorber/1991-emc-pioneer-carbon-based-foam-microwave-absorbers.html>.
- [2] Light reflectance, <http://performativedesign.com/definitions/light/reflectance/>.
- [3] Lattice graph,<https://en.wikipedia.org/wiki/lattice,graph>, May2019.
- [4] Wikipedia article: Scattering parameters, Feb 2020.
- [5] Wikipedia article: Polarization (waves), Jan 2020.
- [6] Michael A. Cole, David A. Powell, and Ilya V. Shadrivov. Strong terahertz absorption in all-dielectric Huygens' metasurfaces. *Nanotechnology*, 27(42), OCT 21 2016.
- [7] Sands Feynman, Leighton. *The Feynman Lectures*, volume 1. Addison-Wesley Publishing Company, Inc., 1963.
- [8] Sands Feynman, Leighton. *The Feynman Lectures*, volume 2. Addison-Wesley Publishing Company, Inc., 1963.
- [9] M.S. Bradley I.F. Almog and V. Bulovic. *The Lorentz Oscillator and its applications*. 2011.
- [10] Yuri Kivshar and Andrey Miroshnichenko. Meta-optics with mie resonances. *Opt. Photon. News*, 28(1):24–31, Jan 2017.
- [11] N. I. Landy, S. Sajuyigbe, J. J. Mock, D. R. Smith, and W. J. Padilla. Perfect metamaterial absorber. *Phys. Rev. Lett.*, 100:207402, May 2008.
- [12] Xinyu Liu, Kebin Fan, Ilya V. Shadrivov, and Willie J. Padilla. Experimental realization of a terahertz all-dielectric metasurface absorber. *Optics Express*, 25(1):191–201, JAN 9 2017.
- [13] Alessandro Vaccari, Antonino Calà Lesina, L. Cristoforetti, A. Chiappini, F. Prudenzano, Alessandro Bozzoli, and Maurizio Ferrari. A parallel computational fdtd approach to the analysis of the light scattering from an opal photonic crystal. *Proc SPIE*, 8781, 05 2013.
- [14] Claire M. Watts, Xianliang Liu, and Willie J. Padilla. Metamaterial electromagnetic wave absorbers. *Advanced Materials*, 24(23):OP98–OP120, 2012.
- [15] Zhi Weng and Yunsheng Guo. Broadband Perfect Optical Absorption by Coupled Semiconductor Resonator-Based All-Dielectric Metasurface. *Materials*, 12(8), APR 2 2019.